A&A 441, 379–389 (2005)
DOI: 10.1051/0004-6361:20053100

Astronomy & Astrophysics

Imaging Saturn's rings with CAMIRAS: thermal inertia of B and C rings

C. Ferrari[1], P. Galdemard[1], P. O. Lagage[1], E. Pantin[1], and C. Quoirin[2]

[1] Laboratoire AIM, Unité Mixte de Recherche No. 7158 CEA-CNRS-Université Paris 7, France
e-mail: cferrari@cea.fr,galdemard@cea.fr,lagage@cea.fr,epantin@cea.fr
[2] Université Paris 6 – Pierre et Marie Curie, France

Received 21 March 2005 / Accepted 11 May 2005

Abstract. Thermal inertias Γ of Saturn's B and C ring particles have been derived from infrared observations using the CAMIRAS camera mounted on the Canada-France-Hawaii Telescope. They are respectively $\Gamma_B = 5^{+18}_{-2}$ J m^{-2} K^{-1} s$^{-1/2}$ and $\Gamma_C = 6^{+12}_{-4}$ J m^{-2} K^{-1} s$^{-1/2}$. Such low values might be characteristic of a frosty and porous regolith fractured by cracks or of very porous particle aggregates. Particles have to be slowly spinning to explain the observed ring temperatures. A large azimuthal asymmetry with an amplitude about 1 K is detected on the West ansa of the B ring. It cannot be explained by a model that considers the ring as a slab of low thermal inertia rapidly warming up to the sunlight after its eclipse into the planetary shadow.

Key words. planetary rings – infrared: solar system – conduction – radiation mechanism: thermal

1. Introduction

Ring particle physical properties, such as bulk density, internal structure, or surface state are poorly known. Ring particles may be aggregates of icy fluffy balls or smooth regular spheres. Depending on their structure, the output of inter-particle collisions, therefore ring evolution, will vary. Their surface and close sub-surface can be probed only indirectly by polarimetry, reflectance, and emittance spectroscopy or by imaging of scattered sunlight. Near-infrared spectra of Saturn's rings show that the main component on the surface is water ice (Pilcher et al. 1970; Puetter & Russel 1977) in its crystalline form (Grundy et al. 1999). The depth of water ice bands implies that characteristic size of the constituent particles are a few tens of microns, most probably measuring the size of surface regolith grains or the surface roughness of the cm-to-m sized Saturn ring particles (French & Nicholson 2000). Polarimetry and imaging of scattered sunlight by ring particles support the idea of irregular surfaces (Esposito et al. 1984). The bulk material is usually assumed to be solid ice with a volume density of 918 kg m^{-3}. Marouf et al. (1983) have deduced, however, a density from radio observations as low as one third of this value but with significant uncertainty.

Ring particles cool down when they cross the planetary shadow and heat up when back in the sunlight. During this transient thermal regime, the surface temperature changes at a rate which depends on its thermal inertia. Compact water ice surfaces of high thermal inertia will suffer only small temperature variations. Fluffy, porous, or frosty regoliths will prevent heat propagation into the particle or will hardly be able to store heat. Temperature changes will be large due to their low thermal inertia.

In order to constrain the thermal inertia and the particle size distribution in Saturn's rings from thermal infrared observations, Aumann and Kieffer (1973) proposed a model of heating and cooling of ring particles. Morrison (1974) gave a lower limit of 40 J m^{-2} K^{-1} s$^{-1/2}$ for the thermal inertia in the B ring, assuming that the particles are larger than 2 cm and using Aumann and Kieffer model figures. Froidevaux et al. (1981) have measured a gradient in brightness temperature of ~8 K ± 4 K for the B ring and ~6 K for the C ring between entry and exit from shadow. They have also observed how the brightness temperature of the B ring varies along the ring (Fig. 6). Qualitative comparison with Aumann's model has led to rejecting a thermal inertia as high as that of solid water ice (2600 J m^{-2} K^{-1} s$^{-1/2}$). A thermal inertia of 13 J m^{-2} K^{-1} s$^{-1/2}$, measured at the same epoch for the Galilean satellites, has been favored instead, with the condition that ring particles are larger than 1 cm. This is in agreement with Morrison's conclusions on the size limit but supports the idea of a lower value for the thermal inertia thanks to more accurate measurements. The Pioneer infrared radiometer was the first instrument onboard a spacecraft to provide data on ring temperatures in the shadow itself. Froidevaux and Ingersoll (1980) reported temperature drops of about 10–15 K in the A and C rings confirming the idea of a low thermal inertia. Observations of C ring shadow were also performed with

the IRIS Voyager infrared spectrometer (Hanel et al. 1981), but no estimate of thermal inertia has been derived.

With such a low thermal inertia, particles should have recovered their equilibrium temperature at the East ansa, a quarter of an orbit after midnight, located at the middle of the planetary shadow. Many observers in the seventies and eighties have not observed any temperature contrast between the East and far West ansae in the A, B, and C rings, with 2 K uncertainty on measurements (Murphy 1972; Nolt et al. 1980; Tokunaga et al. 1980). Nolt et al. (1978) and Froidevaux et al. (1980) did not detect any gradient between ansae except in the C ring, with a values of $\triangle T_{\mathrm{E/W}}$(C ring) = 3.5 K ± 2 K and $\triangle T_{\mathrm{E/W}}$(C ring) = 6 ± 2 K, respectively. This difference has been explained simply by the fact that C ring particles had spent less time back in sunlight after their exit from eclipse (Froidevaux et al. 1980). However some observers (Allen et al. 1971; Murphy et al. 1972; Morrison 1974) have mentioned the existence of such a gradient between both ansae, which they relate either to the cooling of particles in the planetary shadow or to a variation in albedo on the particle surface, the leading side being brighter than the trailing side. There is certainly a thermal gradient between exit from shadow and the East morning ansa for the B and C rings, while the temperature asymmetry between East and West ansae remains uncertain for A and B rings. More recently, thermal IR spectroscopy of Saturn's A and B rings has not detected any temperature gradient between East and West ansae (Lynch et al. 2000), confirming that most of the heating of ring particles in these rings happens before they reach the morning East ansa.

Our objective is to derive quantitative estimates of the thermal inertia of Saturn's main rings. We mounted the CAMIRAS instrument built at the SAp/DAPNIA/DSM/CEA Saclay laboratory on the CFH Telescope to obtain images of Saturn's rings in the mid-infrared domain and to measure full longitudinal temperature profiles of the rings. We then built a simple thermal model to derive the thermal inertia from the observed heating period on the morning East ansa. In this paper, we present the observations performed in July 1999 and March 2000 in Sect. 2. In Sect. 3, a model of particles heating and cooling is proposed to constrain the thermal inertia of ring particles. The thermal inertias for both B and C rings are derived and discussed in Sect. 4. Conclusions and future work are in Sect. 5.

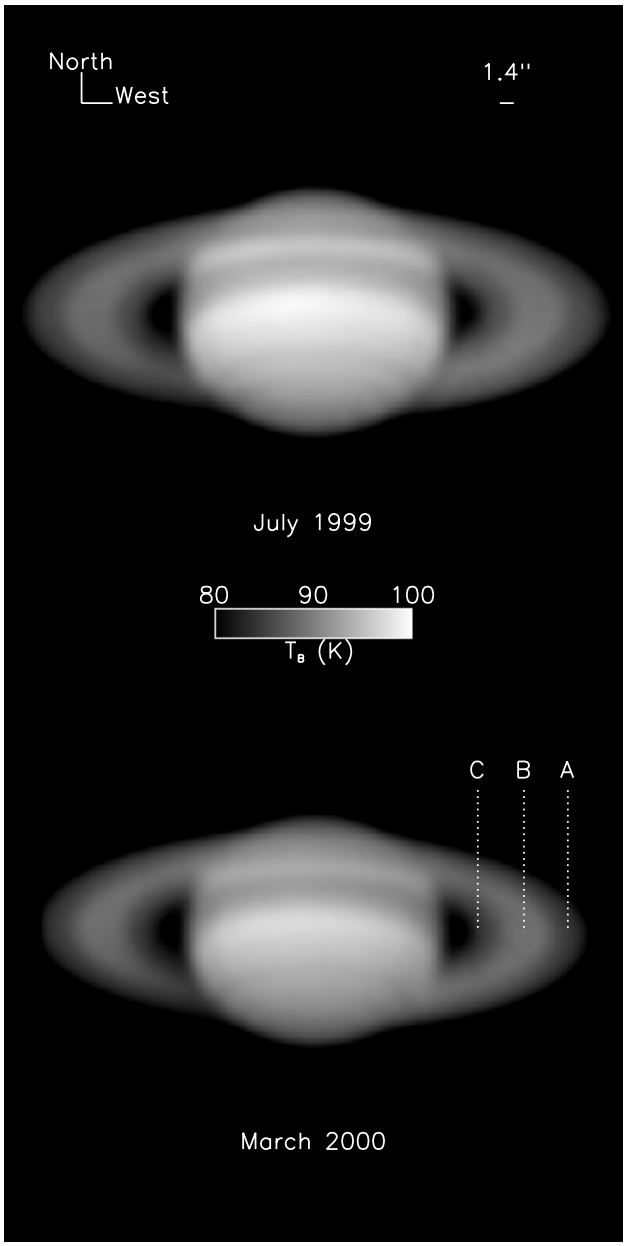

Fig. 1. CAMIRAS images of Saturn and its rings at 20.5 μm. The effective spatial resolution of 1.4″ is plotted on the upper right corner. Ring particles motion is clockwise. The East ansa of the ring and the exit of the shadow are on the left side of the planet.

2. Observations

Saturn's rings were observed in the Q band (20.5 μm), where they are the brightest from the Earth in the mid-infrared. Images contain 128 × 128 pixels with a pixel field of view of approximatively 0.33″. Raw images were processed following classical reduction methods using chopping and nodding techniques to remove bright sky and telescope emissions. They were flat-fielded too (Fig. 1). Sky images were used as flatfield images, as they are the most numerous available. Flatfielding with difference of sky images taken at two different air masses or at two different time exposures give comparable results. The flatfielding step was tested on a series of images where a star is displaced randomly on the detector array. The residual fluctuations on the star flux are about 2%. As our target is systematically moving on the array and hundreds of images co-added, we expect the residual fluctuations at small spatial scale due to pixel non-uniformities to be reduced much below this level. We observed that the temperature of both ansae of the outer A ring increases by 0.6 K symmetrically after flatfielding, mainly due to the correction of vignetting. The detector and photon noises are ≤0.1% of the ring brightness temperature in March data and ≤0.2% in July data. Images were re-centered by a correlation algorithm temporarily using an oversampling in a ratio of 4 pixels to 1. North pole of Saturn was aligned to image columns using available astrometric data and camera orientation data. The alignment was adjusted by fitting ring and planet expected shapes against observed ones. The residual

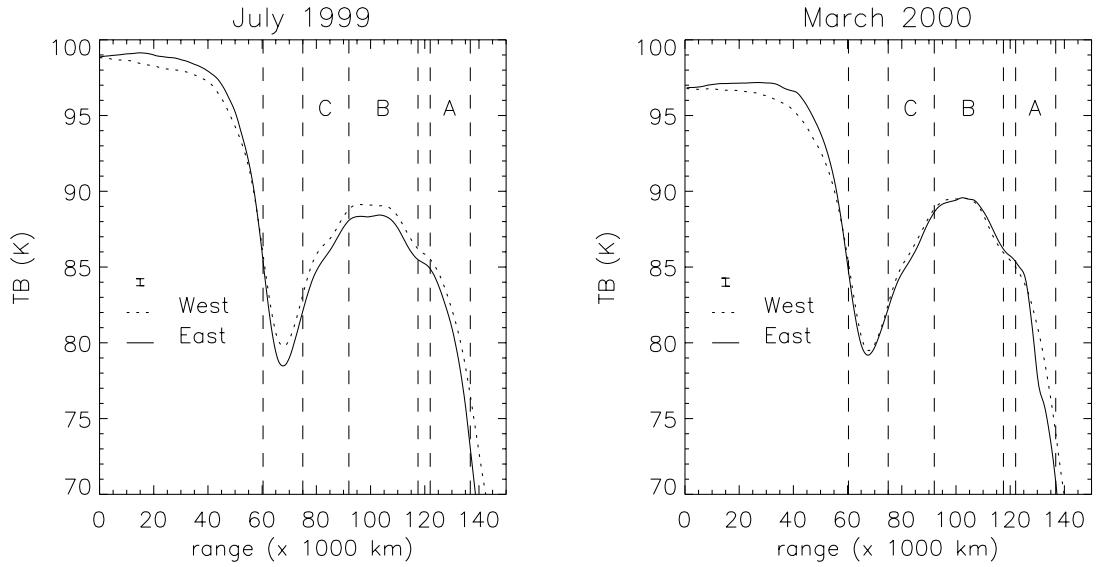

Fig. 2. Radial profiles of Saturn's rings in July 1999 and March 2000. Brightness temperature is given as a function of the distance to Saturn center. Profiles taken on the East and West ansae are overlapping for a better comparison. Error bars represent ±0.3 K (1σ) average uncertainty over the rings. In March 2000, the East ansa is slightly truncated at the edge of the detector array. Vertical dashed lines represent Saturn radius (R_S = 60 330 km) and boundaries of main rings.

relative error on temperature due to orientation uncertainty is ≤0.3%. The equatorial scan of the ring system from East to West ansae (Fig. 2) shows that the astrometric reduction is accurate to less than half a pixel (0.15″). The final error bars on data reflect orientation and noise uncertainties but do not include absolute uncertainty on calibration. Flux calibration was done with the α Tau reference star (Cohen et al. 1995). The specific intensity of the star at 20.5 μm is 1.1417 $\mathrm{Wm^{-2}\,m^{-1}}$. The brightness temperature T_B is directly deduced from the observed flux assuming emissivity of unity, i.e. $I_\nu = B_\nu(T_B)$. This is reasonable for a pure water ice composition at the wavelength of observation. At the epoch of the first CAMIRAS observations, on July 31st, 1999, the Earth and Sun elevations above Saturn ring plane were $B = -20.94°$ and $B' = -19.04°$, with the phase angle 6.2° on the West ansa. The Sun–Saturn distance was 9.35 AU. On March 23rd, 2000, these angles were respectively −20.39°, −21.56°, and 4.7° on the East ansa, at a distance of 9.8 AU.

A, B, and C ring temperatures on the ansae were 82 K, 88.5 K, and 86.5 K in July respectively and 81 K, 89.5 K, and 86 K in March (Fig. 2). The average uncertainty is about 0.3 K for 1 σ level. To be compared with previously cited observations, which are normalized to a Sun–Saturn distance of 9.25 AU, temperatures have to be corrected by $\frac{\Delta T}{T}$ = 0.55% and 2.8%, respectively. The temperatures of A and B rings are in very good agreement with expectations of both monolayer and multilayer thermal models for a solar elevation around 20° (Froidevaux 1981; Kawata 1983). A and B ring normalized temperatures increase with solar elevation, which is compatible with the idea that the physical temperature increases as the solar flux penetrates deeper into the ring layers. The C ring exhibits significantly warmer normalized temperatures (87 K in July 1999 and 88.5 K in March 2000) compared to the value of 82 K expected by models and previous observations. But they remain compatible with the Nolt et al. (1978) measurement of 87.7 K in the C ring at solar elevation $B' = 6.5°$. They also slightly increase with solar elevation contrary to the currently accepted picture that this ring is thin enough for the inter-particle shadowing effect to be negligible at these solar elevations. The elevation of the observer is almost constant, but the solar elevation has increased by nearly 2° in between. A slight increase in the brightness temperature of the rings might then be expected in March 2000, when solar rays enter deeper into Saturn's rings and heat up ring particles more efficiently. But Saturn is also farther away from the Sun by 0.44 UA, which somewhat counterbalances this effect so that comparable fluxes are expected in both data sets. No East–West asymmetry were detected in the March 2000 observations (Fig. 2). In July data, a 0.7 K (0.8%) asymmetry systematically appeared in each ring but it remained within the error bars (0.3% for astrometry and 0.2% for 1σ noise level, i.e. 0.3 K). We cannot confirm the existence of a thermal gradient between East and West ansae in the C ring as seen in previous data.

Azimuthal profiles of B and C ring are displayed in Fig. 3. Points were extracted every 10 degrees in the longitudinal direction inside the B ring and every 12 degrees in the C ring to be independent, given the limited spatial resolution of 1.4″. Because the A ring is most sensitive to IR flat-fielding and optical distortions, we were not able to extract an azimuthal profile with reasonable error bars. The Earth was near maximum elongation on the West ansa in July 1999 so that the entry into the shadow could be seen. In March 2000, the exit of the shadow could be observed despite the moderate East elongation of the Earth (Fig. 3). Data around noon were not plotted because they were contaminated with Saturn infrared emission. In the B ring, the temperature gradient between the exit from the shadow (longitude 30°) and the East ansa (longitude 90°) was 5.5 K ± 0.7 K in March 2000. It was about

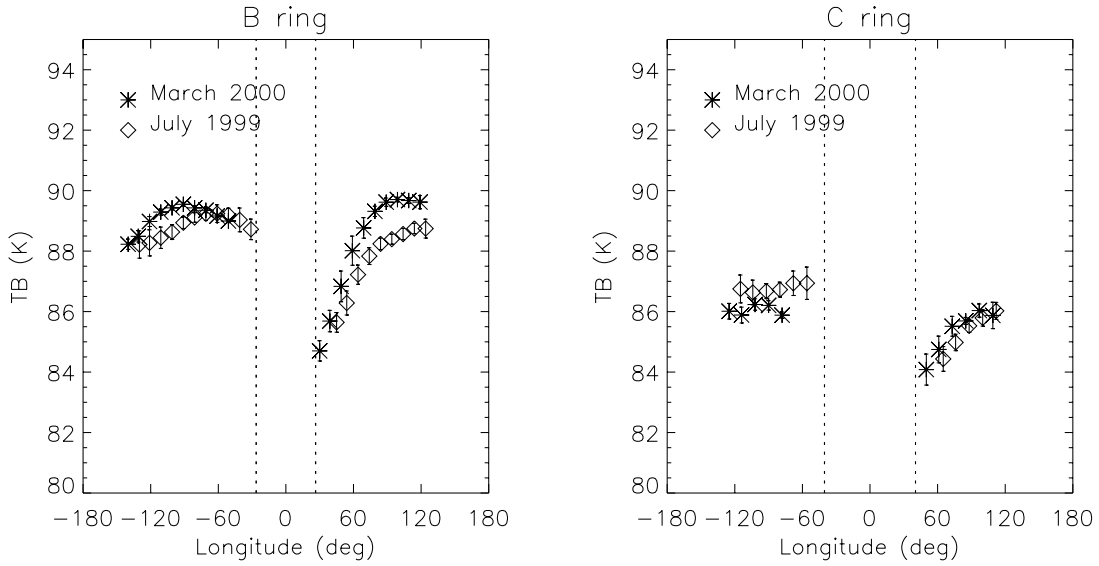

Fig. 3. Azimuthal brightness temperature profiles of B and C rings in July 1999 and March 2000. Longitude 0° is located at midnight in the middle of the shadow. The East (morning) ansa is at longitude 90°, noon at ±180° and West (afternoon) ansa at longitude −90°. Error bars represent 1σ uncertainty. Vertical dashed lines represent the shadow limits on the rings. The shadow extent does not change significantly between epochs at the longitudinal scale of this figure. The ellipsoid shape of Saturn was taken into account.

3.0 K ± 0.8 K in July as the first five minutes of heating cannot be observed. Particles had recovered most of their initial temperature at East ansa. In the C ring, a maximum gradient of 2.0 K ± 0.7 K was observed between exit from the shadow and East ansa in March 2000 (Fig. 3). It fell down to 1.5 K ± 0.8 K in July 1999. The measurements at the exit of the shadow were certainly contaminated by the planet due to the limited spatial resolution.

A slight azimuthal asymmetry of 1.0 K ± 0.7 K could be seen on the West ansa (longitude –140 to –50) of the B ring in July, its amplitude was about 1.3 K ± 0.4 K in March 2000. It peaked at $-60\pm20°$ in July and at $-90\pm15°$ in March. After the West ansa (longitude −90°), a ground-based observer would be looking at the face of a spherical particle, which is illuminated both by direct sunlight and planet infrared radiation at the same time. If slowly spinning with low thermal inertia, the brightness temperature of the sphere will increase regularly with azimuth and peak just before entry into the shadow. This suggestion meant to explain the observed azimuthal asymmetry has to be more widely explored by including spherical spinning particles in our model. No significant azimuthal asymmetry other than the one due to the heating after the eclipse could be observed in the C ring.

3. Eclipse thermal model

It is complex to build a thermal model of particles heating and cooling across the planetary shadow, as many important phenomena and physical properties have to be taken into account. Ring particles will react differently to transient thermal regime according to (i) the structure and composition of their surface; (ii) their spin rate and obliquity; (iii) their size; or (iv) their vertical dynamics along their orbit. The flux from the heating sources will reach the particle surface with variable efficiency depending on the vertical dynamics of the particle and the vertical structure of the ring. Several assumptions were introduced here to be able to constrain the thermal inertia of ring particles.

3.1. Energy balance

The brightness temperature of a ring T_B differs from the particle temperature T_S due to interparticle shadowing and ring-filling factor. Aumann & Kieffer (1973) have related both temperatures with an anisotropy index Q, such that $T_B = Q^{1/4}T_S$, to take the emission function of individual particles and the filling factor into account. This model implicitly assumes a monolayer structure of the ring. In the case of very low optical depth, $Q = Q$(particle) and $Q = 1$ for very large optical depth. The anisotropy of the emission function of ring particles depends on their spin rate, axis, and thermal inertia.

In the present paper, the ring is also assumed to spread in a monolayer as described by Froidevaux (1981). The brightness temperature is related to the particle temperature by:

$$B_\nu(T_B) = \epsilon_{ir}(1 - e^{-\tau})C(B, \tau)\frac{B_\nu(T_S)}{\mu} \leq B_\nu(T_S) \quad (1)$$

as the number of particles seen from elevation B varies as $1/\mu$ where $\mu = \sin B \cdot C(B, \tau)$ is the fractional emitting area of the particle visible from elevation B above the ring plane for a ring optical depth τ. All particles have the same surface temperature T_S. The fractional area of the ring filled with particles is $(1-e^{-\tau})$. $B_\nu(T)$ is the intensity of a blackbody at temperature T and frequency ν.

Table 1. Definitions of variables.

A_V	Ring particle bolometric Bond albedo
A_S	Saturn bolometric Bond albedo =0.342
B	Earth elevation above the ring plane
B'	Solar elevation above the ring plane
C_H	Specific heat ($J\,kg^{-1}\,K^{-1}$)
$C(B', \tau)$	Particle fractional lit area
$C(B, \tau)$	Particle fractional visible area
D_{AU}	Sun-Saturn distance in astronomical units
ϵ_{ir}	Infrared emissivity of ring particles, $\epsilon_{ir} = 1$
F_1	Direct sunlight
F_2	Sunlight reflected by Saturn
F_3	Thermal radiation from Saturn
F_4	Sunlight scattered by nearby particles
Γ	Thermal inertia ($J\,m^{-2}\,K^{-1}\,s^{-1/2}$)
K	Thermal conductivity ($W\,m^{-1}\,K^{-1}$)
μ	sin(B)
Ω_P	Solid angle of the lit planet hemisphere
Ω_P'	Solid angle of the planet hemisphere
Ω_R	Solid angle subtended by all nearby particles
p	Porosity of the particle regolith
z	Depth in particle
ρ_0, ρ	Volume density of the regolith (ρ_0 = 918 kg m^{-3})
S, σ	Solar constant =1370 $W\,m^{-2}$, Stefan constant
τ	Ring optical depth
T_B	Ring brightness temperature
T_S	Particle surface temperature
T_P	Saturn planet effective temperature, T_P = 95 K
ω	Particle mean motion

A particle at distance a from Saturn center receives energy from different sources, i.e. the Sun, Saturn, and the nearby particles. The energy balance, away from the shadow is:

$$(1-A_V)\frac{S}{D_{AU}^2}C(B',\,\tau) + A_S(1-A_V)\frac{S}{D_{AU}^2}\frac{\Omega_P}{\pi} + \frac{\sigma T_P^4 \Omega_P'}{\pi} + A_V(1-A_V)\frac{S}{D_{AU}^2}C(B',\,\tau)\frac{\Omega_R}{4\pi} = F_1 + F_2 + F_3 + F_4 = \left(1-\frac{\Omega_R}{4\pi}\right) f\epsilon_{ir}\sigma T_S^4. \quad (2)$$

Definitions of variables are given in Table 1. Ring particles have a bolometric Bond albedo A_V. They are located at distance D_{UA} from the Sun, which emits S $W\,m^{-2}$ at 1 AU. The first term F_1 on the left corresponds to the fraction of sunlight absorbed by the particle after it has been screened by nearby particles. The second term F_2 figures the sunlight scattered by the planet on the particle and absorbed. The third term F_3 is the Saturn infrared emission absorbed by the particle. The visible light scattered by nearby particles, which takes the inter-particle mutual shadowing into account, is represented by the fourth term F_4 on the left. Minor modifications have been added in Eq. (2) compared to Froidevaux's model. The dependence in longitude of the direct solar F_1 and of the planet lit hemisphere inputs F_2 are now taken into account. All but the infrared contributions are zero in the shadow. Also the solid angles Ω_P and Ω_P' subtended by the planet are systematically divided by 2 for the B ring as particles might not see a complete Saturn hemisphere because of the ring thickness. The right-hand term represents the thermal emission of the particle corrected from the absorbed infrared flux from nearby emitting particles.

The inter-particle shadowing is represented in this model by the fractional area $C(B', \tau)$ of the particle visible from elevation B' above the ring plane. It is dissociated from the anisotropy of the particle emission function, which is described by rotation factor f. Formulation of $C(B', \tau)$ has been provided by Froidevaux for two viewing geometries of a monolayer of ring particles regularly distributed along a reseau and producing minimum and maximum shadowing factors. We prefered, however, to use his experimental curve of $C(B', \tau)$ derived from laboratory measurements of the shadowed fractional area in random configurations of spherical balls, mentioned as the random shadowing case.

Ground-based observations of Saturn are limited to small phase angles. In this viewing geometry, only the day side of particles is observed. It corresponds to the warmest point of slowly rotating particles (assuming the thermal inertia is small), or to the average temperature for the faster ones, then isothermal (assuming their pole of rotation is not facing the Sun at any time). The anisotropy of the emission function is described here by rotation factor f. $F = 2$ for a slow rotating particle, which emits mainly over one hemisphere, and $f = 4$ for a fast rotating isothermal particle, which emits over 4π sr. All particles are then supposed to have the same spinning behavior in this ring, an assumption which might be true in Saturn's rings only for the population of large particles. Centimeter-sized particles are gravitationally scattered by the larger ones and show a large dispersion in spin rate (Salo 1987; Richardson 1994). The total solid angle Ω_R subtended by the eight closest neighbours is $\Omega_R = 6(1-e^{-\tau})$ as the blocking area is $\pi r_S^2/4d^2 = 1-e^{-\tau}$. This assumes that the four closest particles are located at distance 2d and that the four left are at distance $2\sqrt{2}d$. Average optical depths τ of the B and C rings are 1.4 and 0.1, respectively (Hanel et al. 1981; Spilker et al. 2002; Esposito et al. 1984).

Contribution of the different heating sources varies with the ring distances and optical depth (Fig. 4). The main heating source is, of course, the Sun (F_1). The particles in the thiner C ring are warmer than the B ring because the absorbed flux is greater due to weaker inter-particle shadowing. The infrared contribution from the planet on ring particles (F_3) is larger in the C ring as it is closer to the planet. Including infrared and visible contributions from the closest particles ($\frac{\Omega_R}{4\pi} f\epsilon_{ir}\sigma T_S^4$ and F_4) significantly raises the temperature in the B ring compared to the C ring, as particles are closer together in that thick ring. The infrared contribution of the neighbours is progressively decreasing in the shadow as particles are cooling together. The way this flux decreases in the shadow is unknown a priori as the surface temperature of particles has not been solved yet.

The contribution of Saturn's visible hemisphere F_2 is larger in the C ring too. C ring particles absorb much more flux than

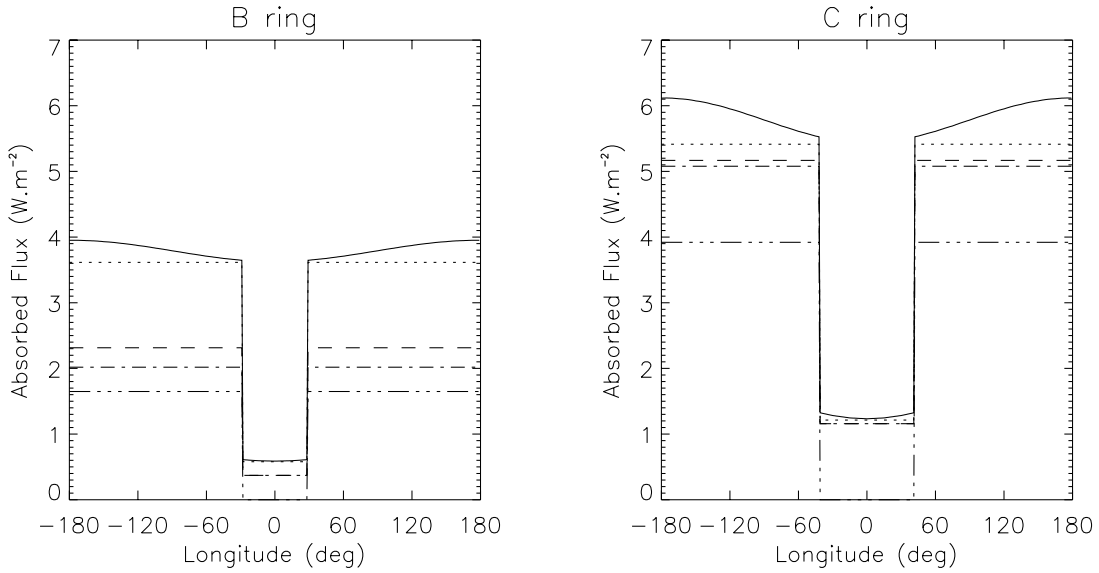

Fig. 4. Absorbed fluxes of B and C rings as a function of ring longitude and heating sources for Bond albedo $A_V = 0.5$ and $f = 2$ at July 1999 epoch. $(-\cdots)$ F_1, $(-\cdot-)$ $F_1 + F_3$, $(--)$ $F_1 + F_3 + F_4$, (...) $F_1 + F_3 + F_4$+infrared neighbours, (solid line) $F_1 + F_2 + F_3 + F_4$ +infrared neighbours. Longitude is zero at midnight; West ansa (W) is located at $-90°$ and East ansa (E) at $90°$.

B ring particles due to their lower distance from the planet and the limited mutual shadowing. This creates an azimuthal asymmetry in the rings which peaks at noon (Fig. 4). But the shape of this azimuthal asymmetry is model-dependent. Our model indeed computes the temperature of a flat ring element, which receives all the contributions at the same time, but this is not the case for a real spherical particle. At noon, F_2 is absorbed by the face of the sphere, which is invisible to a ground-based observer. Then, in the case of a slow spinning particle, the present asymmetry due to F_2 can never be seen in fact. If the particle is rapidly spinning in comparison with the orbital period and is of moderate thermal inertia, this energy input may be visible just after noon by the observer. At other longitudes, the F_2 contribution becomes negligible. The flux F_3 suffers the same problem but does not induce an azimuthal asymmetry here, as it is constant along the azimuth. Its contribution in the shadow is very important for both rings and far from negligible in the C ring. The F_2 contribution of the Saturn visible hemisphere will be neglected from now on, as it is quite negligible and produces an artificial azimuthal asymmetry in flux (and then in temperature), which is not real. It is confirmed in the fit between data and model as the residuals are much worse when F_2 is included. F_3 will be included as its contribution is not negligible on average along the orbit. A new model which takes into account the spherical shape of particles, their spin rate and orientation should be built to bypass these drawbacks.

3.2. Heat diffusion

Many processes like radiation, conduction, or convection can be involved in the transfer of energy through a surface regolith in transient regime. They depend on its structure, temperature, composition and phase. Both radiation and convection may play an important role in a porous regolith. But at these temperatures, both can be neglected in first approximation, and heat transfer by conduction only is considered. The incident fluxes are absorbed at the very surface. For a periodic thermal system with fundamental harmonic ω, here the mean motion of particles around Saturn, the conservation of energy at depth z translates into the heat diffusion equation:

$$\frac{1}{z^2}\frac{\partial}{\partial z}\left(z^2\frac{\partial T}{\partial z}\right) = \frac{1}{\omega}\frac{\partial T}{\partial t} \tag{3}$$

assuming axisymmetry of the problem in spherical coordinates, homogeneity and isotropy of thermal properties Depth z is normalized here to the thermal skin $\delta = \frac{\Gamma}{\rho C_H \sqrt{\omega}}$, i.e. the depth of penetration of the thermal wave. At the center of the particle, the heat flow is supposed to be zero.

Thermal inertia $\Gamma = \sqrt{K\rho C_H}$ is the global physical property which controls both the temperature variations at the surface of ring particles and the capacity of the sub-surface to store heat. It mainly depends on thermal conductivity K, as volume density ρ and specific heat C_H vary less with the nature of the material. The boundary condition for the heat flow at the surface is:

$$F_T - f\epsilon_{ir}\sigma T_S^4\left(1 - \frac{\Omega_R}{4\pi}\right) = -\Gamma\sqrt{\omega}\frac{\partial T}{\partial z}(z=0) \tag{4}$$

where $F_T = \sum F_i$ is the total energy per unit cross-sectional area absorbed by the particle. The thermal inertia measures the resistance of a material to changes in incident heat flux (Fig. 5). For a material made of solid water ice ($\Gamma = 2600$ J m^{-2} K^{-1} s$^{-1/2}$), crossing the planetary shadow does not influence the surface temperature, which equals the average temperature T_0. As thermal inertia decreases, the regolith becomes less insulating and temperature variations appear in the shadow and at the exit when particles are back in the sunlight.

The specific heat C_H is the amount of heat necessary to increase the temperature of 1 m^{-3} of solid material in 1 s by 1 K. It characterizes the ability of the material to store heat. Experimental studies by Klug et al. (1991) show that it

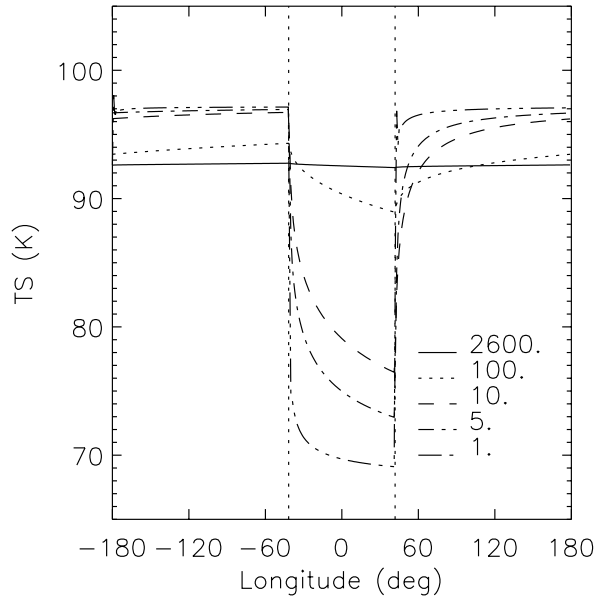

Fig. 5. Azimuthal variation of the surface temperature as a function of thermal inertia Γ (J m^{-2} K^{-1} s$^{-1/2}$). The particle is located at a = 84 000 km from Saturn, A_V = 0.5, f = 2 and ρ = 918 kg m^{-3}. Calculations are made for the viewing geometry of the July 1999 epoch. In this case, T_0 = 92.6 K and C_H = 783.7 J kg^{-1} K^{-1}. All incident fluxes but F_2 have been included.

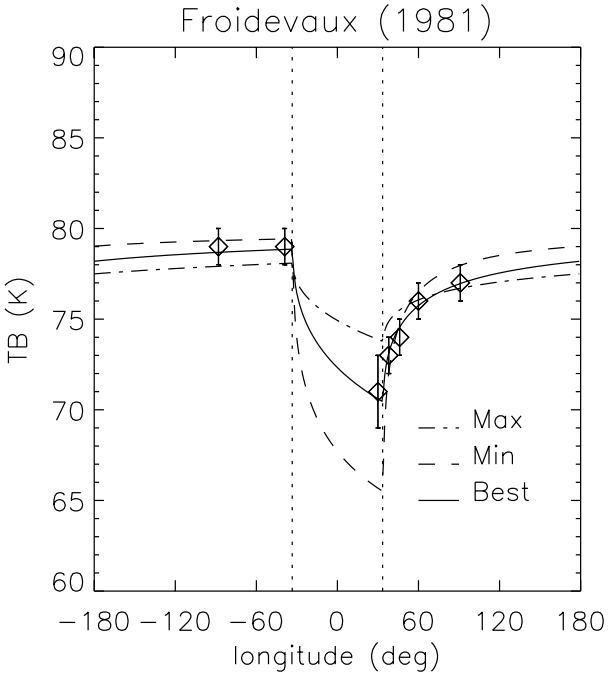

Fig. 6. Best fit of the B ring data of Froidevaux et al. (1981) obtained with our eclipse model for f = 2. Thermal inertia is $\Gamma = 16^{+14}_{-11}$ J m^{-2} K^{-1} s$^{-1/2}$ and Bond albedo $A_V = 0.48^{+0.04}_{-0.07}$ at 3σ. At the epoch B = 12.8°, B' = 10° and the phase angle is 6.3° on the East ansa. "Max" and "Min" show the temperature for the limit values Γ and A_V = 0.48.

increases only by a factor of about 1.7 between the Ih crystalline phase of water ice and its low density amorphous phase, at a ring temperature of 100 K. It also depends on temperature. For crystalline water ice, it follows the law $C_H = 7.49T + 90$ where T is the temperature of the material (Klinger 1981). As temperature might significantly differ from B to C ring due to different inter-particle shadowing, we have introduced this temperature dependence in our model. However, instead of using the inside temperature T, the average surface temperature over a period $T_0 = (\frac{\langle F_T \rangle}{\epsilon_{ir}\sigma})^{1/4}$ is used and $C_H = 7.49\,T_0 + 90$. Its value is then determined for an epoch of observation and a ring.

The thermal conductivity K is the amount of heat transfered in 1s due to a thermal gradient of 1 K/m in the material. In other words, it controls the heat flow, given a thermal gradient according to Fourier's law. K depends on the composition of the solid phase and more importantly on its structure. The more there are areas of contact between grains of the regolith, for example, the better the heat can propagate by conduction and the higher K. The thermal conductivity may then decrease because of fractures in a compacted regolith or because of porosity.

Particles are supposed to be much larger than the thermal skin depth, i.e. $r_S \geq 5\delta$. Saturn's ring particles are known to be cm-to-m sized with a continuous power-law size distribution $n(r)\mathrm{d}r = r^{-q}\mathrm{d}r$, where $q \sim 3$ on average and with minimum and maximum sizes of about 3–30 cm and 10–20 m, respectively, in the C and B rings, respectively (French & Nicholson 2000, and references therein). Smaller dust particles are absent (Dones et al. 1993; Doyle et al. 1989; Cooke 1991). The validity of this assumption is checked a posteriori.

The diffusion Eq. (3) inside the particle is solved with a Crank-Nicolson algorithm. This finite difference implicit scheme, which is second order accurate in both space and time, has been chosen to insure stability and convergence for a wide range of Fourier numbers, even if it may be slower than any other simpler scheme. The boundary condition (4) is nonlinear in T_S and has been linearized. The surface temperature curve T_S on 360° longitude is re-calculated until the average emitted flux equals to the average absorbed flux. The tolerance on this criterion is 10^{-4}. The relative accuracy of equality $T_S(t = 0) = T_S(t = T)$ is about 10^{-5} for the values of the thermal inertia used in this paper.

4. Results and discussion

Azimuthal profiles of brightness temperature are fitted here to the model by minimizing the distance $\Sigma(T_{B,\mathrm{mod},i} - T_{B,\mathrm{obs},i})^2/\sigma_i^2$ by varying the Particle Bond albedo A_V and the thermal inertia Γ. $T_{B,\mathrm{mod}}$ and $T_{B,\mathrm{obs}}$ are the modeled and observed brightness temperatures and σ_i the uncertainty on each point. Having the Bond albedo as a free parameter simply allows us to fix the initial equilibrium temperature before the eclipse. Its value is very dependent on the sources considered, and the small uncertainty on the result reflects uncertainty on the data only. Its absolute value is model-dependent.

Our eclipse model was fitted first to Froidevaux observations of the B ring (1981, Table 2). The thermal inertia was constrained to be $\Gamma = 16^{+14}_{-11}$ J m^{-2} K^{-1} s$^{-1/2}$ for a Bond albedo $A_V = 0.48^{+0.04}_{-0.07}$ at 3σ (Fig. 6). It is close to the qualitative estimate made by Froidevaux of a thermal inertia comparable to that of the Galilean satellites. As can be seen in Fig. 6,

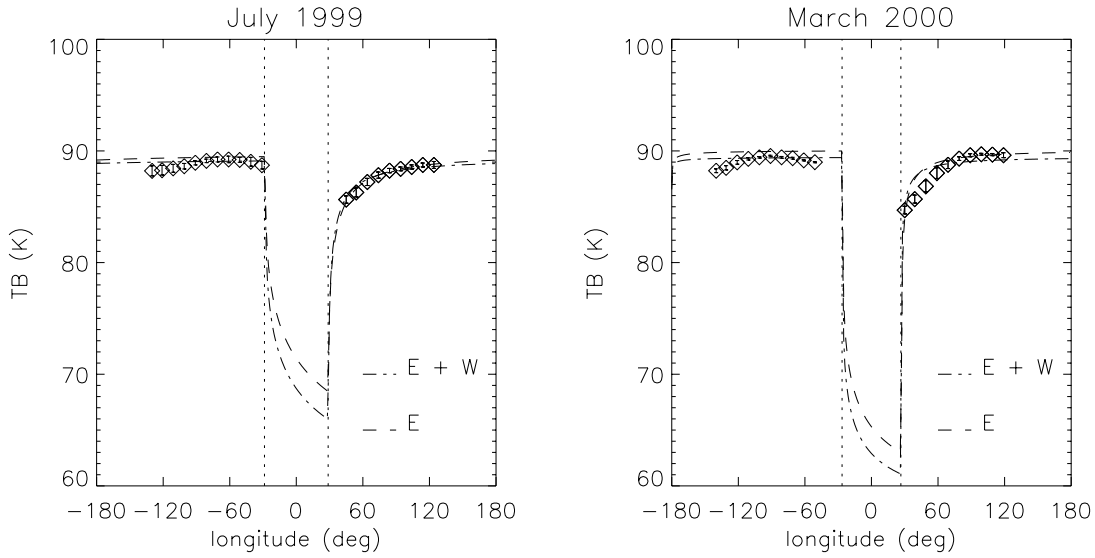

Fig. 7. Brightness temperature azimuthal profile of the B ring at range $a = 105\,000$ km ($1.74R_S$) in July 1999 and March 2000. Best fits (3σ) are represented in case of: (E) fit with east ansa data only, (E+W) fit with east and west ansae data.

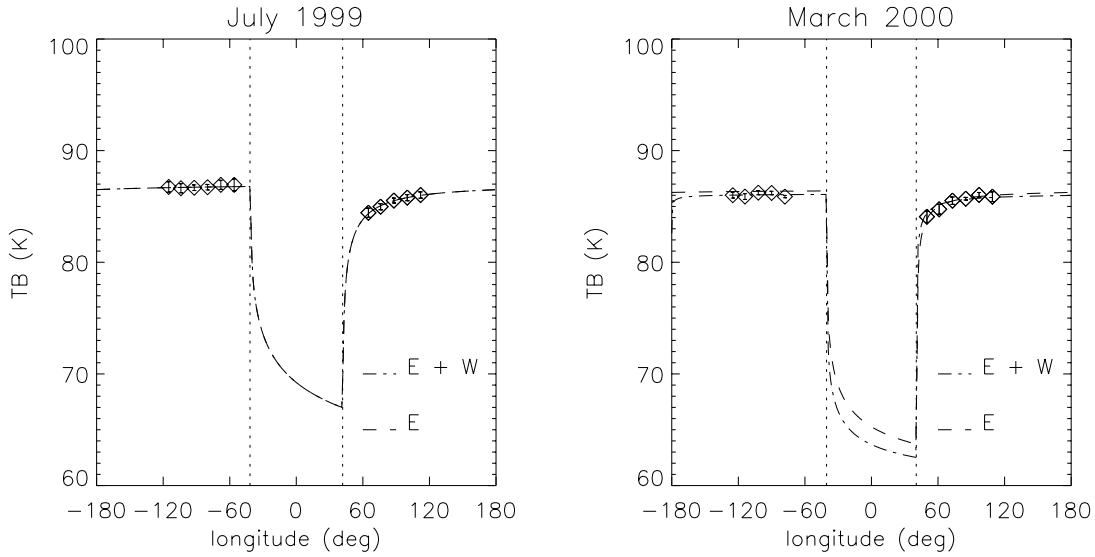

Fig. 8. Best fits of brightness temperature azimuthal profile of the C ring at range $a = 84\,000$ km ($1.39R_S$) in July 1999 and March 200. See Fig. 7 for details.

the brightness temperature can decrease by more than 15 K in the planetary shadow when the thermal inertia is on the order of 5 to 20 J m^{-2} K^{-1} s$^{-1/2}$. This is compatible with Pioneer measurements of a 10–15 K drop in the shadow for A and C rings (Froidevaux & Ingersoll 1980).

Two separate fits were run on the CAMIRAS data, for each ring at each epoch: the first one takes data of both ansae into account, the second one only fits data of East ansa. This is to account for the fact that the model fails to reproduce the azimuthal asymmetry on the West ansa of the B ring and not on the East ansa. Azimuthal temperature curves of the best fits for the B ring are shown in Fig. 7. The model fails to reproduce the observed ring temperatures with $f = 4$, which means that the observed temperatures are too high for the particles to be almost isothermal emitters in the frame of our model. For $f = 2$, B ring values for thermal inertia and Bond albedo are summarized in Fig. 9. The Bond albedo values found at both July 1999 and March 2000 epochs are very consistent. This means that the model is capable of treating the seasonal variations in temperature due to variations in the sun elevation and distance. Thermal inertias are found to be very low, about a few J m^{-2} K^{-1} s$^{-1/2}$, i.e. about three orders of magnitude lower than the thermal inertia of solid water ice. Thermal inertia is significantly lower in March compared to July, but the residuals of the fit in March are very bad. The model does not seem to be able to reproduce the observed slope in temperature on the East ansa (Fig. 7). Given the residuals for the B ring in March, these solutions were rejected. On July 1999, the average Bond albedo of the B ring is $A_V = 0.48^{+0.02}_{-0.04}$ and the average thermal inertia is $\Gamma_B = 5^{+18}_{-2}$ J m^{-2} K^{-1} s$^{-1/2}$.

Fits to the C ring data are better since there are no bright asymmetries on the West ansa that cannot be reproduced by

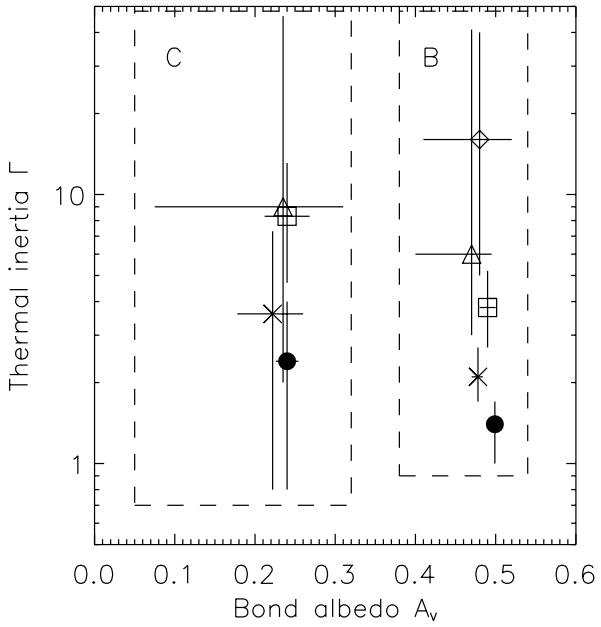

Fig. 9. Thermal inertias Γ and Bond albedos A_V of B and C rings. Solutions are found by using data from: (triangle) CAMIRAS, July 1999 with East ansa only; (square) CAMIRAS, July 1999 with both ansae; (cross) CAMIRAS, March 2000 with East ansa only; (full circle) CAMIRAS, March 2000 with both ansae; (losange) Froidevaux 1981(see Fig. 6). Errors bars are given at 3σ level.

the model (Fig. 8). Also for this ring, no solution for the Bond albedo is found if $f = 4$. This, once again, rejects a ring of quasi-isothermal particles. For $f = 2$, results are summarized in Fig. 9. Bond albedos are again very consistent between epochs, and are significantly lower than are those of B ring. Thermal inertias are also very low in this ring and almost equal to that of the B ring. They were marginally lower in March 2000 than in July 1999. The average Bond albedo of the C ring is $A_V = 0.23^{+0.04}_{-0.06}$, and its average thermal inertia is $\Gamma_C = 6^{+12}_{-4}$ J m^{-2} K^{-1} s$^{-1/2}$.

The bolometric Bond albedoes are compatible with the most recent estimates obtained at visual wavelengths by Cuzzi & Estrada (1998) using Voyager images, i.e. 0.46 and 0.18 for B and C rings, respectively. They were obtained for highly anisotropic emitters exclusively, which is new in the case of the C ring. Given the small thermal inertia, particles have to be slowly spinning to emit by one hemisphere only ($f = 2$). Froidevaux (1981) could obtain a fit between his monolayer-model, slowly spinning particles ($f = 2$) and C ring data only for a bolometric Bond albedo of 0.55, which was too high compared to the expected value of 0.25 at epoch (Esposito et al. 1984, Table 6). A lower albedo value was possible for $f = 4$, i.e. in case of very small particles, fast rotation or high thermal inertia. A large spin rate corresponds to a large velocity dispersion in the ring and a vertical thickness that is not compatible with the monolayer. The monolayer model was rejected for the C ring for this reason (Esposito et al. 1984). The C ring brightness temperature derived from CAMIRAS observations is about 7 K above the value expected by the model for $A_V = 0.55$. This shift in temperature by itself explains the low values of the Bond albedo obtained here. Monolayer, slowly spinning particles, and low albedo are no longer incompatible for the C ring. The monolayer structure for the C ring should be reconsidered then, especially as observations of waves in this ring have since suggested a vertical thickness of less than 1 m (Rosen 1989), i.e. a monolayer structure for a population whose effective size is about 2 m (French and Nicholson 2000).

Thermal inertias are found to be very low. Many other icy bodies in the solar system also exhibit comparable thermal inertias, yet slightly larger. Ground-based observations of Europa have given thermal inertia as low as 17 J m^{-2} K^{-1} s$^{-1/2}$ for low albedo regions ($A_V < 0.6$, Blaney et al. 1999). The thermal inertia of higher albedo regions of Europa, of the other Galilean satellites or of saturnian satellites like Rhea, Dione or Tethys range between 30 and 70 J m^{-2} K^{-1} s$^{-1/2}$ (Spencer 1989, 1992). The thermal inertias of Chiron or Asbolus Centaurs have been very recently estimated at 10 J m^{-2} K^{-1} s$^{-1/2}$ or less (Fernandez et al. 2002; Groussin et al. 2000).

A low thermal inertia $\Gamma = \sqrt{K\rho C_H}$ means that material on the surface of a particle cannot store heat or else it insulates the subsurface. For a compacted surface, the volumic density might be close to $\rho_0 = 918$ kg m^{-3} and its specific heat C_H close to solid water ice value, i.e. $C_H = 741$ or 845 J kg^{-1} K^{-1} for temperatures in the B and C ring, respectively. The low thermal inertia would then be due to an insulating regolith with low thermal conductivity K. For the average thermal inertias of B and C rings, K would be on the order of 4×10^{-5} W m^{-1} K^{-1}. This is five orders of magnitude smaller than the expected thermal conductivity for solid water ice. The standard formula given by Klinger (1981) for crystalline compact water ice is $K_0 = 567/T_0$, i.e. ~ 6 W m^{-1} K^{-1} on average for B and C rings at our epochs. With such low thermal conductivities, the thermal skin depth δ is limited to 0.4 mm, given the mean motions of B and C ring particles. This is small compared to the typical size of Saturn's ring particles. The hypothesis we made to consider particles large compared to the thermal skin depth is reasonable then. Near-infrared spectroscopy suggests that Saturn's rings particles are covered with water ice frost with a typical grain size smaller than 50 μm (Puetter & Russel 1977; Molina et al. 1992). More detailed modeling of ring spectra by Poulet et al. (2002) tends to confirm the predominence of such grain size even if some fraction of larger grains (100–200 μm) has to be present. The thermal skin depth might then be much larger than the typical regolith grain size. In these conditions the measured thermal inertia is the thermal inertia of the regolith and not that of the grain material. This depth is much larger than the electrical skin depth $\delta_E = \lambda/4\pi n_k$ where λ is the wavelength of observation and n_k the imaginary part of the refractive index of crystalline water ice. From laboratory experiments at 100 K (Bertie 1969), $n_k(\lambda = 20\ \mu\text{m}) \sim 10^{-1}$. Then $\delta_E \sim 20\ \mu\text{m} \ll \delta$. Therefore the observed temperature is actually the surface temperature at 20.5 μm.

Kouchi et al. (1992) have produced laboratory measurements of the thermal conductivity of amorphous water ice at temperatures around 130 K while slowly depositing a thin film on a cold metal substrate. The mean thermal conductivity of the deposit (mixing in fact amorphous and crystalline water ice) has been found to decrease with decreasing

deposition rate, from 10^{-1} to 10^{-5} $\mathrm{W\,m^{-1}\,K^{-1}}$ with rate from 10^{-5} to 10^{-9} $\mathrm{cm\,s^{-1}}$. Most measurements are below 10^{-4} $\mathrm{W\,m^{-1}\,K^{-1}}$ for deposition rate below 10^{-6} $\mathrm{cm\,s^{-1}}$. This low thermal conductivity might not be due to the amorphous ice structure but simply to defects in the ice deposit (Kouchi et al. 1992; Bunch et al. 1998), like cracks that would prevent heat diffusion while keeping the porosity low. The porosity is indeed limited in their samples as the infrared absorptivity indicates a mean density of about 900 $\mathrm{kg\,m^{-3}}$ $\sim \rho_0$. These experimental results are very interesting, as they give a proper range for thermal conductivity and a plausible origin due to cracks. Cracks might indeed grow easily under the surfaces of particles which are eroded by inter-particle collisions. Fractures may be created at the impact point and ejecta from the collision be compressed on the surface, creating a compacted frosty regolith (Weidenschilling et al. 1984). Thermal stress during nights and days of the spinning particle (possibly few times 10 K-gradient in one orbit) or during the crossing of the planetary shadow may also create fractures on the surface, as would highly energetic particles which break molecules bonds on the surface and fragilize the frosty regolith cover (Borderies et al. 1984).

The porosity p of the regolith, if likely, is unknown. It may directly affect the heat transfer into the medium by reducing the available mass participating to heat conduction. Porosity p lowers the heat capacity $\rho C_\mathrm{H} = (1-p)\rho_0 C_\mathrm{H}$ by a factor $(1-p)$. The effective thermal conductivity of this porous material is also affected as the area of contacts, through which heat flows, are reduced. In this case $K = (1-p)K_0$, where K_0 is the thermal conductivity of the regolith grains. For high porosity like $p = 0.9$, the thermal inertia $\Gamma = (1-p)\sqrt{\rho_0 C_\mathrm{H} K_0}$ corresponds to a thermal conductivity $K_0 \sim 4 \times 10^{-3}$ $\mathrm{W\,m^{-1}\,K^{-1}}$. This is still three orders of magnitudes below the thermal conductivity of water ice. So, porosity, even high, cannot alone explain such low thermal inertias, as far as the theory of effective medium is valid for our case.

The thermal inertias are low, and particles have recovered most of their pre-eclipse temperature on the morning east ansa. Other azimuthal temperature variations are visible in the B ring on the West afternoon ansa, which cannot be reproduced by the present model. Also some systematic discrepancy appears between thermal inertias measured in July 1999 and March 2000. These may be due to some phase effect not handle by our model. A possible origin for such azimuthal temperature variations and apparent phase effect is under investigation (Ferrari & Leyrat 2005).

5. Conclusions

It has been suspected for a long time that the thermal inertia of Saturn's main rings is low. This paper provides the first quantitative estimates for the B and C rings: $\Gamma_\mathrm{B} = 5^{+18}_{-2}$ $\mathrm{J\,m^{-2}\,K^{-1}\,s^{-1/2}}$ and $\Gamma_\mathrm{C} = 6^{+12}_{-4}$ $\mathrm{J\,m^{-2}\,K^{-1}\,s^{-1/2}}$, respectively. They are very low, three orders of magnitude less than the thermal inertia of solid water ice. The thermal inertia of the first millimeters of the particles surface was sounded. If covered by a regolith, its porosity cannot explain such a low thermal inertia by itself. Cracks created by thermal stress or by inter-particle collisions may prevent the heat flow and perfectly insulate the subsurface from large variations in incident heating flux. This would easily explain the low thermal inertia, as laboratory measurements tend to demonstrate. Data on the A ring were not workable. A full understanding of the origin of such low thermal inertias is beyond the purpose of this paper. Energy transport in regolith depends on grain size, optical and thermal properties of the grains, the compactness of the regolith, and on the possible existence of fractures that prevent heat propagation. Many models have been developed recently to treat energy transport in such regoliths and should certainly be applied to the study of particles in Saturn's rings, in a context where surfaces are exposed to frequent collisions. Particles have to be highly anisotropic emitters ($f = 2$) to be able to produce the observed ring temperatures.

CAMIRAS data show that previously undetected azimuthal temperature asymmetries are present in the West ansa of the B ring, at a place where temperature is expected to be about constant due to the low thermal inertia of particles. Our work also shows that the C ring temperatures can be easily reproduced by a model that assumes it is a monolayer of slowly rotating particles with low albedo and low thermal inertia. Also, if distributed in a monolayer, B ring particles can hardly be quasi-isothermal.

In the next months, the CIRS spectrometer onboard the CASSINI spacecraft will send back unique data on the heating and cooling of A, B, and C rings with very diverse viewing geometries. It will undoubtedly provide new insights on the azimuthal temperature asymmetries and their variations with viewing angles. Direct observations of the shadow will also help to better constrain their thermal inertia and probably their rotational properties.

Acknowledgements. Many thanks to P. Masse and R. Jouan for their fundamental contribution to the success of this observing campaign. This work was supported by the Programme National de Planétologie and Centre National d'Études Spatiales.

References

Allen, D. A., & Murdock, T. L. 1971, Icarus, 14, 1
Aumann, H. H., & Kieffer, H. H. 1973, ApJ, 186, 305
Bunch, T. E., Wilson, M. A., & Pohorille, A. 1998 Techn. Rep. NASA Ames Research Center
Bertie, J. E., Labbé, H. J., & Whalley, E. 1969, J. Chem. Phys., 50, 4501
Blaney, D. L., Goguen, J. D., Veeder, G. J., Matson, D. L., & Johnson, T. V. 1999, BAAS, 31, 1171
Borderies, N., Goldreich, P., & Tremaine, S. 1984, in Planetary Rings, ed. R. Greenberg, & A. Brahic (Tucson: The University of Arizona Press) 713
Cohen, M., Witteborn, F. C., Walker, R. G., Bregman, J. D., & Wooden, D. H. 1995, AJ, 110, 275.
Cooke, M. 1991, Ph.D. Thesis, Cornell University
Cuzzi, J. N., & Estrada, P. R. 1998, Icarus, 132, 1
Dones, L., Cuzzi, J. N., & Showalter, R. 1993, Icarus, 105, 184
Doyle, L. R., Dones, L., & Cuzzi, J. N. 1989, Icarus, 80, 104
Esposito, L. W., Cuzzi, J. N., Holberg, J. B., et al. 1984, in Saturn, ed. T. Gehrels, & M. S. Matthews (Tucson: The University of Arizona Press) 463

Ferrari, C., & Leyrat, C. 2005, A&A, submitted
Fernandez, Y. R., Jewitt, D. C., & Sheppard, S. S. 2002, AJ, 123, 100
French, R. G., & Nicholson, P. D. 2000, Icarus, 145, 502
Froidevaux, L. 1981, Icarus, 46, 4
Froidevaux, L., & Ingersoll, A. P. 1980, J. Geophys. Res., 85, 5929
Froidevaux, L., Matthews, K., & Neugebauer, G. 1981, Icarus, 46, 18
Groussin, O., Peschke, S., & Lamy, P. L. 2000, BAAS, 32, 1031
Grundy, W. M., Bue, M. W., Stansberry, J. A., Spencer, J. R., & Schmitt, B. 1999, Icarus, 142, 536
Hanel, et al. 1981, Science, 212, 192
Kawata, Y. 1983, Icarus, 56, 453
Kawata, Y., & Irvine, W. M. 1975, Icarus, 24, 472
Klinger, J. 1980, Science, 209, 271
Klinger, J. 1981, Icarus, 47, 320
Lynch, D. K., Mazuk, A. L., Russell, R. W., & Hackwell, J. A. 2000, Icarus, 146, 43
Klug, D. D., Whalley, E., Svensson, E. C., Root, J. H., & Sears, V. F. 1991, Phys. Rev. B, 44, 841
Kouchi, A., Greenberg, J. M., Yamamoto, T., & Mukai, T. 1992, ApJ, 388, L73
Marouf, E. A., Tyler, G. L., Zebker, H. A., Simpson, R. A., & Eshelman, V. R. 1983, Icarus, 54, 189
Molina, A., Moreno, F., Kidger, M., & Ortiz, J. L. 1992, A&A, 298, 624
Morrison, D. 1974, Icarus, 22, 57
Murphy, R. E. 1972, ApJ, 181, L87
Murphy, R. E., Cruikshank, D. P., & Morrison, D. 1972, BAAS, 4, 358
Nolt, I. G., Tokunaga, A., Gillett, F. C., & Caldwell, J. 1978, ApJ, 181, L87
Nolt, I. G., Barrett, E. W., Caldwell, J., et al. 1980, Nature, 283, 842
Pilcher, C. B., Chapman, C. R., Lebofsky, L. A., & Kieffer, H. H. 1970, Science, 167, 1372
Pollack, J. B. 1975, Space Sci. Rev., 18, 3
Poulet, F., & Cuzzi, J. N. 2002, Icarus, 160, 350
Puetter, R. C., & Russel, R. W. 1977, Icarus, 32, 37
Richardson, D. 1994, MNRAS, 269, 493
Rosen, P. A. 1989, Scientific Report No. D845-1989-1, Stanford University
Salo, H. 1987, Icarus, 70, 37
Spencer, J. R., & Moore, J. M. 1992, Icarus, 99, 261
Spencer, J. R., Lebofsky, L. A., & Sykes, M. V. 1989, Icarus, 78, 337
Spilker, L. J., Wallis, B. D., Ferrari, C., & Pearl, J. C. 2002, BAAS, 33, 1096
Tokunaga, A., Caldwell, J. , & Nolt, I. 1980, Nature, 287, 212
Weidenschilling, S. J., Chapman, C. R., Davis, D. R., & Greenberg, R. 1984, in Planetary Rings, ed. R. Greenberg, & A. Brahic (Tucson: The University of Arizona Press), 367